Mechanism of selective benzene hydroxylation catalyzed by iron-containing zeolites

Benjamin E. R. Snyder[a,1], Max L. Bols[b], Hannah M. Rhoda[a], Pieter Vanelderen[a,b], Lars H. Böttger[a], Augustin Braun[a], James J. Yan[a], Ryan G. Hadt[a,2], Jeffrey T. Babicz Jr.[a], Michael Y. Hu[c], Jiyong Zhao[c], E. Ercan Alp[c], Britt Hedman[d], Keith O. Hodgson[a,d], Robert A. Schoonheydt[b,3], Bert F. Sels[b,3], and Edward I. Solomon[a,d,3]

[a]Department of Chemistry, Stanford University, Stanford, CA 94305; [b]Department of Microbial and Molecular Systems, Centre for Surface Chemistry and Catalysis, Katholieke Universiteit Leuven, B-3001 Leuven, Belgium; [c]Advanced Photon Source, Argonne National Laboratory, Argonne, IL 60439; and [d]Stanford Synchrotron Radiation Lightsource, SLAC National Accelerator Laboratory, Stanford University, Menlo Park, CA 94025

Edited by Alexis T. Bell, University of California, Berkeley, CA, and approved October 18, 2018 (received for review August 22, 2018)

A direct, catalytic conversion of benzene to phenol would have wide-reaching economic impacts. Fe zeolites exhibit a remarkable combination of high activity and selectivity in this conversion, leading to their past implementation at the pilot plant level. There were, however, issues related to catalyst deactivation for this process. Mechanistic insight could resolve these issues, and also provide a blueprint for achieving high performance in selective oxidation catalysis. Recently, we demonstrated that the active site of selective hydrocarbon oxidation in Fe zeolites, named α-O, is an unusually reactive Fe(IV)=O species. Here, we apply advanced spectroscopic techniques to determine that the reaction of this Fe(IV)=O intermediate with benzene in fact regenerates the reduced Fe(II) active site, enabling catalytic turnover. At the same time, a small fraction of Fe(III)-phenolate poisoned active sites form, defining a mechanism for catalyst deactivation. Density-functional theory calculations provide further insight into the experimentally defined mechanism. The extreme reactivity of α-O significantly tunes down (eliminates) the rate-limiting barrier for aromatic hydroxylation, leading to a diffusion-limited reaction coordinate. This favors hydroxylation of the rapidly diffusing benzene substrate over the slowly diffusing (but more reactive) oxygenated product, thereby enhancing selectivity. This defines a mechanism to simultaneously attain high activity (conversion) and selectivity, enabling the efficient oxidative upgrading of inert hydrocarbon substrates.

zeolites | spectroscopy | catalysis

The direct conversion of benzene to phenol remains an outstanding challenge in modern chemistry (1). Fe zeolites exhibit remarkable performance in this application, hydroxylating benzene catalytically with 95+% selectivity for phenol—even at high levels of conversion (30–45%) (2–6). This is the critical step in the AlphOx process of Panov, implemented in a Solutia pilot plant (2–5). Catalyst deactivation at elevated temperature remains a crucial problem (4, 7, 8). Mechanistic insight could resolve this issue, and provide a blueprint for developing selective oxidation catalysts with high reactivity and selectivity. However, despite three decades of effort, direct experimental data clarifying the catalytic mechanism are limited (9). We recently showed the active site of selective hydrocarbon hydroxylation, called α-Fe(II) (2), is a mononuclear S = 2 square planar Fe(II) center (10, 11). α-Fe(II) is activated by nitrous oxide to form α-O (2), a mononuclear square pyramidal S = 2 Fe(IV)=O intermediate with a constrained coordination geometry that imparts exceptional reactivity, enabling H-atom abstraction from CH_4 at room temperature (10, 11). In this study, we investigate the single-turnover reactivity of α-O with C_6H_6 using advanced spectroscopic techniques from bioinorganic chemistry. Spectroscopic data show the reduced α-Fe(II) active site is regenerated following single turnover. The phenol product is thus released from the active site quantitatively at room temperature, but not overoxidized. At the same time, we find a small fraction of partially oxidized, deactivated Fe(III)-phenolate sites are generated. These data, coupled to density-functional theory (DFT) calculations, define a catalytic mechanism leading to high activity (conversion) and selectivity, along with a competing mechanism leading to catalyst deactivation.

Results and Discussion

Defining the Product of Single Turnover. Direct experimental data tracking the state of the α-O active site in its reaction with benzene are lacking. We therefore used Mössbauer spectroscopy as a quantitative probe of iron speciation in iron-exchanged zeolite beta (Fe-BEA) under single-turnover conditions. As shown in Fig. 1*A*, reacting α-O in Fe-BEA (gray trace) with C_6H_6 vapor at room temperature results in the quantitative formation of a new species labeled α-C_6H_6 (red trace) with 6K Mössbauer parameters characteristic of high spin (S = 2) Fe(II) (isomer shift, IS; quadrupole splitting, QS; IS = 1.30, QS = 3.90), but distinct from those previously defined for α-Fe(II) (precursor to α-O; blue trace) (10, 11). The larger quadrupole splitting of α-C_6H_6 indicates this site no longer has the square planar geometry of α-Fe(II), suggesting an axial ligand is now present.

Significance

Fe zeolites are heterogeneous catalysts that show potential in a number of important industrial applications, including the selective partial oxidation of methane to methanol at room temperature, and the selective conversion of benzene to phenol. There are practical limitations associated with Fe-zeolite catalysts that may be resolved with mechanistic insight; however, reliable experimental data on Fe zeolites are limited. This study defines the mechanism of selective benzene hydroxylation catalyzed by Fe zeolites, clarifying the relationship between active site structure and catalytic performance (activity, selectivity). Mechanistic insight from this study represents an important step toward synthetic control over function in selective hydrocarbon oxidation catalysis.

Author contributions: B.E.R.S., R.A.S., B.F.S., and E.I.S. designed research; B.E.R.S., M.L.B., H.M.R., P.V., L.H.B., A.B., J.J.Y., R.G.H., J.T.B., M.Y.H., J.Z., and E.E.A. performed research; B.E.R.S., B.H., K.O.H., R.A.S., B.F.S., and E.I.S. analyzed data; and B.E.R.S., R.A.S., B.F.S., and E.I.S. wrote the paper.

The authors declare no conflict of interest.

This article is a PNAS Direct Submission.

[1]Present address: Department of Chemistry, University of California, Berkeley, CA 94720.

[2]Present address: Division of Chemistry and Chemical Engineering, California Institute of Technology, Pasadena, CA 91125.

[3]To whom correspondence may be addressed. Email: robert.schoonheydt@biw.kuleuven.be, bert.sels@biw.kuleuven.be, or edward.solomon@stanford.edu.

This article contains supporting information online at www.pnas.org/lookup/suppl/doi:10.1073/pnas.1813849115/-/DCSupplemental.

Published online November 14, 2018.

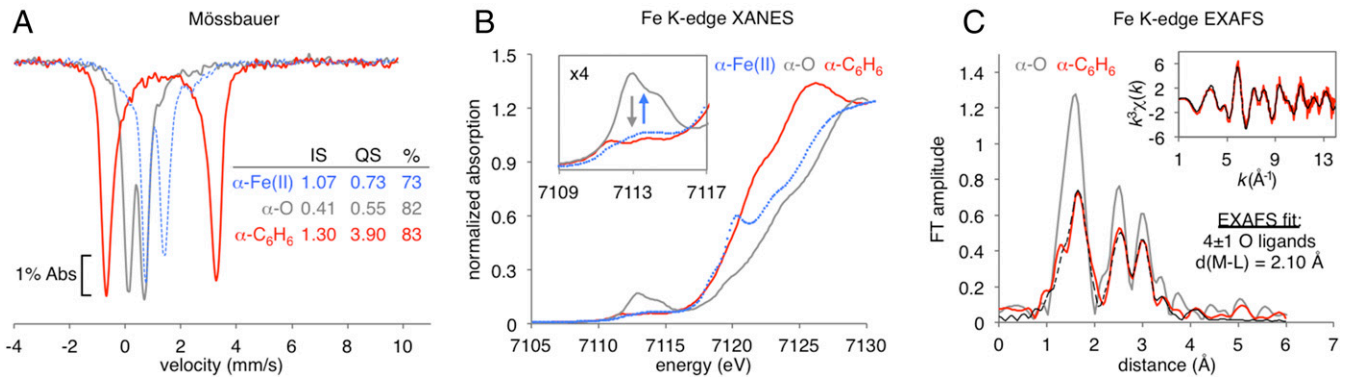

Fig. 1. (*A*) Low temperature (6K) ^{57}Fe Mössbauer spectrum of α-O in Fe-BEA (82%, gray trace), compared to data collected after its reaction with C_6H_6, forming α-C_6H_6 (83% red trace). Past data (11) from the reduced α-Fe(II) active site are included for reference (73%, blue trace). (*Inset*) The associated Mössbauer parameters are reported. (*B*) Fe K-edge X-ray absorption near-edge spectra of α-O (gray trace) and α-C_6H_6 (red trace), showing an ∼3-eV downshift in the rising edge coupled to loss of the intense preedge features of α-O (*Inset*). Past data (11) from α-Fe(II) are included for reference (blue trace). (*C*) Comparison of FT EXAFS spectra of α-O (gray trace) and α-C_6H_6 (red trace, with fit in dashed black). (*Inset*) The EXAFS spectrum of α-C_6H_6 (experimental data: red; fit: dashed black), with the first shell fit summarized below. The full EXAFS fit is presented in *SI Appendix*, Fig. S2.

To define the ligation of α-C_6H_6, we employed a combination of Fe K-edge X-ray absorption spectroscopy (XAS) coupled to ^{57}Fe nuclear resonance vibrational spectroscopy (NRVS). NRVS is a synchrotron-based technique that selectively probes vibrations of Fe sites in metalloenzymes and zeolites (11, 12). Importantly, NRVS and XAS are sensitive to S = 2 Fe(II) centers, which can be difficult (or impossible) to resolve in optical absorption, resonance Raman (rR), and electron paramagnetic resonance spectroscopy. As shown in the X-ray absorption near-edge region in Fig. 1*B*, the reaction of α-O (gray trace) with C_6H_6 (red trace) results in loss of the intense α-O preedge features at 7,110–7,115 eV (*Inset*), as well as a downshift in the rising edge energy by ∼3 eV. These changes are consistent with reduction of α-O to an Fe(II) species distinct from α-Fe(II) (blue trace, with a low-energy 1s–4p transition at 7,120 eV that is characteristic of square planar geometry) (11). In the extended X-ray absorption fine structure (EXAFS) region in Fig. 1*C*, the Fourier transform (FT) shows a loss of first-shell intensity moving from α-O (gray) to α-C_6H_6 (red). Comparing the first-shell EXAFS fits of α-C_6H_6 in Fig. 1*C* and of α-O from Snyder et al. (11) shows this is due to loss of the short 1.63-Å scattering path from the reactive terminal oxo ligand (see *SI Appendix*, Fig. S2 for full EXAFS fits). The first coordination sphere of α-C_6H_6 was fit with 4 ± 1 oxygen ligands at 2.10 Å. However, the EXAFS fit does not clarify the nature of the axial ligand. (See *SI Appendix*, Fig. S2; this ligand could contribute to the 2.10-Å shell or, alternatively, be weakly bound and not significantly contribute to the experimental data.)

To resolve this ambiguity, we directly synthesized candidates for α-C_6H_6 by binding either phenol (product) or C_6H_6 (substrate, present in excess under reaction conditions) to α-Fe(II). As shown in *SI Appendix*, Fig. S1, in each case this leads to quantitative conversion of α-Fe(II) to a new S = 2 Fe(II) species with Mössbauer parameters that are highly similar to α-C_6H_6. However, XAS and NRVS data presented in Fig. 2 show significant differences for benzene- and phenol-ligated α-Fe(II). FT EXAFS data in Fig. 2*A* show excess first-shell intensity for the phenol-bound site (black trace; see 1–2-Å region) relative to α-C_6H_6 (red trace). The EXAFS fit given in the inset indicates this is due to the presence of a fifth oxygen ligand at 2.09 Å. The X-ray absorption near edge structure (XANES) region presented in *SI Appendix*, Fig. S2 shows the phenol-bound site also does not reproduce the α-C_6H_6 preedge or rising edge. Finally, as shown in Fig. 2*B*, the phenol-bound site (black trace) does not reproduce the distribution of NRVS intensity for α-C_6H_6 (red trace) in the 0–250-cm^{-1} region, which contains FeL_5 core modes that are highly sensitive to coordination geometry (11). In this region, α-C_6H_6 shows a distinct peak at 165 cm^{-1}, while the phenol-bound site has a plateau from 165 to 210 cm^{-1}. The experimental Mössbauer, EXAFS, and NRVS data of the phenol-bound site are reproduced by the S = 2 Fe(II) DFT model presented in *SI Appendix*, Fig. S3. Alternatively, EXAFS data in Fig. 2*C*, NRVS data in Fig. 2*D*, and XANES data in *SI Appendix*, Fig. S2 demonstrate the spectroscopic features of C_6H_6-ligated

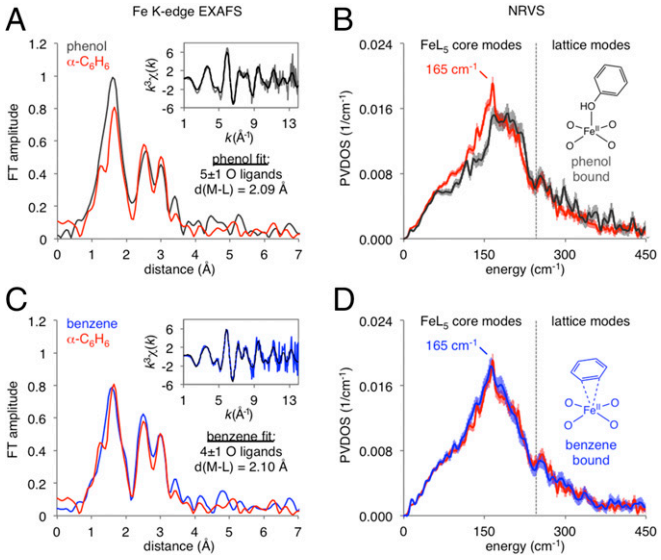

Fig. 2. (*A*) Comparison of FT EXAFS of α-C_6H_6 (red trace) and phenol-bound α-Fe(II) (dark-gray trace). (*Inset*) The phenol-bound k^3-weighted EXAFS is shown (solid gray, fit in dashed black), with the first shell fit parameters given below. (*B*) Comparison of NRVS spectra of α-C_6H_6 (red trace) and phenol-bound α-Fe(II) (dark-gray trace). A structural model of the phenol-bound site is illustrated at the right of the figure, based on correlation of spectroscopy to DFT (*SI Appendix, SI Methods*). (*C*) Comparison of FT EXAFS of α-C_6H_6 (red trace) and benzene-bound α-Fe(II) (blue trace). (*Inset*) The benzene-bound k^3-weighted EXAFS is shown (solid red, fit in dashed black), with the first shell fit parameters given below. (*D*) Comparison of NRVS spectra of α-C_6H_6 (red trace) and benzene-bound α-Fe(II) (blue trace). A structural model of the benzene-bound site, based on correlation of spectroscopy to DFT (*SI Appendix, SI Methods*), is illustrated at the right of the figure.

α-Fe(II) (blue traces) overlay with the features of α-C_6H_6 (red traces). The experimental Mössbauer, EXAFS, and NRVS spectroscopy of α-C_6H_6 are reproduced by an S = 2 DFT model of α-Fe(II) with a weakly bound π-η^2-C_6H_6 ligand (see *SI Appendix*, Fig. S3 for detail). As shown in *SI Appendix*, Fig. S4, the C_6H_6 ligand desorbs from α-C_6H_6 at room temperature, consistent with a weak bonding interaction.

The quantitative conversion of α-O to the substrate-bound reduced active site at room temperature has significant mechanistic implications. α-C_6H_6 is not a reaction intermediate, and its formation requires α-Fe(II) to first release the phenol product before binding the excess C_6H_6 in the reactant stream. These results contradict earlier studies suggesting product desorption from the active site is rate limiting (13, 14), and/or driven by subsequent activation of N_2O (2, 14). High temperatures are therefore not required to regenerate the active site, but do assist in the subsequent desorption of phenol from the zeolite lattice [see temperature-programmed desorption (TPD) data in *SI Appendix*, Fig. S5]. The absence of overoxidized products (2, 3) indicates the released phenol does not go on to react with α-O. Interestingly, α-O does react directly with phenol vapor at room temperature to form diphenols—see *SI Appendix*, Fig. S6 and ref. 15. This suggests the benzene substrate is able to outcompete the phenol product, despite its lower activation toward electrophilic aromatic substitution reactions. The reactivity of α-O is therefore different from other mononuclear Fe(IV)=O intermediates: α-O achieves high levels of selectivity (95+%) at high levels of conversion (40+%) (6), while other Fe(IV)=O intermediates attain lower levels of selectivity (0–70%) at lower levels of conversion (<10%) (16–18). The clean regeneration of the α-Fe(II) active site following aromatic hydroxylation also raises an important contrast to methane hydroxylation in Fe zeolites, which is not catalytic (9), and where past Mössbauer studies show single-turnover results in a heterogeneous distribution of Fe species (*SI Appendix*, Fig. S7) (10). DFT studies presented below clarify the unique features of α-O leading to its unusually high reactivity and selectivity in aromatic hydroxylation.

A Mechanism Leading to Catalyst Deactivation. The regeneration of α-Fe(II) following aromatic hydroxylation in Fe-BEA contrasts with studies of Fe-ZSM-5, where phenolate-ligated products are proposed (19–22). A C_6H_6/α-O formed spectroscopic product with a broad absorption (Abs) band at 13,900 cm^{-1} has been identified in Fe-ZSM-5, assigned as a binuclear Fe(III)-phenolate species based on rR data (20). This is proposed to be either a catalytic intermediate, a poisoned state of the active site, and/or a precursor to coke formation (19–23). We used a range of spectroscopies to clarify the nature of this putative Fe(III) phenolate and its relation to the α-O active site. Mössbauer spectra in *SI Appendix*, Fig. S8 show the reaction of C_6H_6 with Fe-ZSM-5 parallels the Fe-BEA reaction, resulting in near-quantitative formation of a single Fe(II) product, with <5% Fe(III) present. However, as shown in Fig. 3, this also results in the 13,900-cm^{-1} Abs band assigned to an $Fe(III)_2$ phenolate by Xia et al. (20) (Fig. 3*A*).

Tuning a laser into the 13,900-cm^{-1} Abs feature enhances a number of Raman vibrations shown in Fig. 3*B*, with frequencies and intensities consistent with those in ref. 20. Reacting ^{18}O-labeled α-O (see ref. 24 and *Materials and Methods*) with C_6H_6 results in the rR isotope shifts given in parentheses in Fig. 3*B*, which are diagnostic of a bound phenolate ligand. (An analogous 15,200-cm^{-1} Abs feature forms in Fe-BEA—see *SI Appendix*, Fig. S8. Issues with fluorescence precluded rR studies of this system.) Incorporation of the ^{18}O label indicates the phenolate ligand is correlated with the active site (i.e., unrelated to spectator sites).

We used variable-temperature variable-field magnetic circular dichroism (VTVH-MCD) (9, 25) to define the electronic structure of this phenolate-bound species. As shown in Fig. 3*C*, the 13,900-cm^{-1} room-temperature (RT) Abs band resolves into two components at 11,600 cm^{-1} and 13,300 cm^{-1} in 3K MCD spectroscopy. VTVH-MCD isotherms collected from these bands overlay within error, suggesting they derive from the same species. The 11,600-cm^{-1} VTVH-MCD isotherms in Fig. 3*D* require a spin-Hamiltonian fit with an S = 5/2 ground state, consistent with a high-spin mononuclear Fe(III) phenolate [but not an oxo- or hydroxo-bridged 2Fe(III) site, which would have an integer-spin, likely singlet ground state (26)]. Compared with other mononuclear S = 5/2 Fe(III) phenolates, the 647-cm^{-1} Fe-O_{C6H5} stretching frequency from rR is high [typically 570–620 cm^{-1} for S = 5/2 Fe(III) phenolates] (27, 28), indicating a strong binding interaction. Finally, the reaction of α-O with phenol results in >95% regeneration of Fe(II) (*SI Appendix*, Fig. S6), and the formation of diphenols (15). The small amount of Fe(III) phenolate that forms during the benzene reaction is therefore unrelated to small contributions from overoxidation. Site-selective spectroscopy therefore characterizes the geometric and electronic structure of this S = 5/2 Fe(III) phenolate, and shows this is a poisoned state of the α-Fe(II) active site generated during productive turnover. The absence of an Fe(III) signal in Mössbauer indicates <5% of sites are poisoned following single turnover, while analysis of diffuse reflectance UV-vis (DR-UV-vis) band intensities indicates >0.2% poisoning (see *Materials and Methods* for detail). This would lead to 20–100% deactivation after 100 turnovers. DFT calculations presented below suggest phenolate poisoning occurs via H-atom loss from a bound catalytic intermediate.

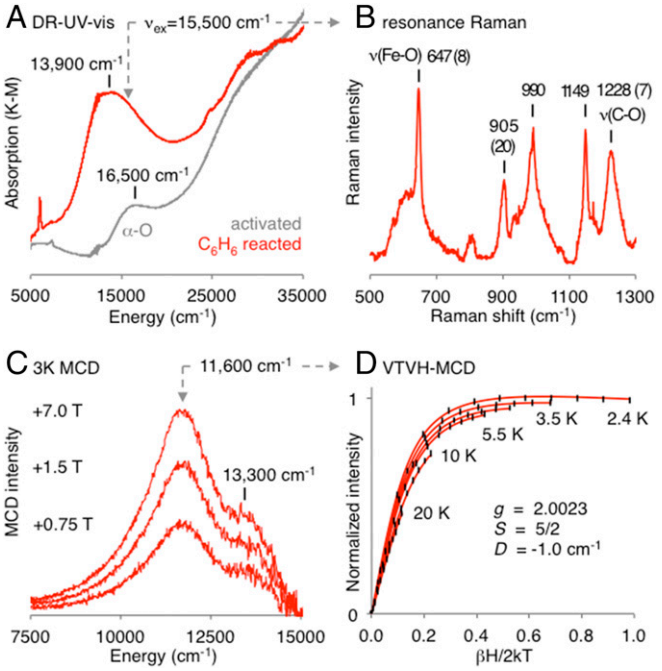

Fig. 3. (*A*) DR-UV-vis spectra of α-O in Fe-ZSM-5 (gray) and α-C_6H_6 (red), showing the appearance of an intense 13,900-cm^{-1} band. (*B*) rR data from laser excitation into the high-energy shoulder of the 13,900-cm^{-1} band, showing vibrations with frequencies and corresponding ^{18}O isotope shifts (given in parentheses) characteristic of a phenolate ligand. The Fe-O and C-O stretching modes are indicated. (*C*) Low temperature (3K) variable-field MCD spectra of C_6H_6-reacted Fe-ZSM-5. (*D*) VTVH-MCD isotherms from the 11,600-cm^{-1} MCD band (±1-σ error bars in black; spin Hamiltonian fit in red), and associated spin Hamiltonian parameters.

A Mechanism Enabling High Reactivity and Selectivity. To define features of α-O contributing to its high reactivity and selectivity in aromatic hydroxylation, we constructed a DFT reaction coordinate that cleanly regenerates the reduced α-Fe(II) active

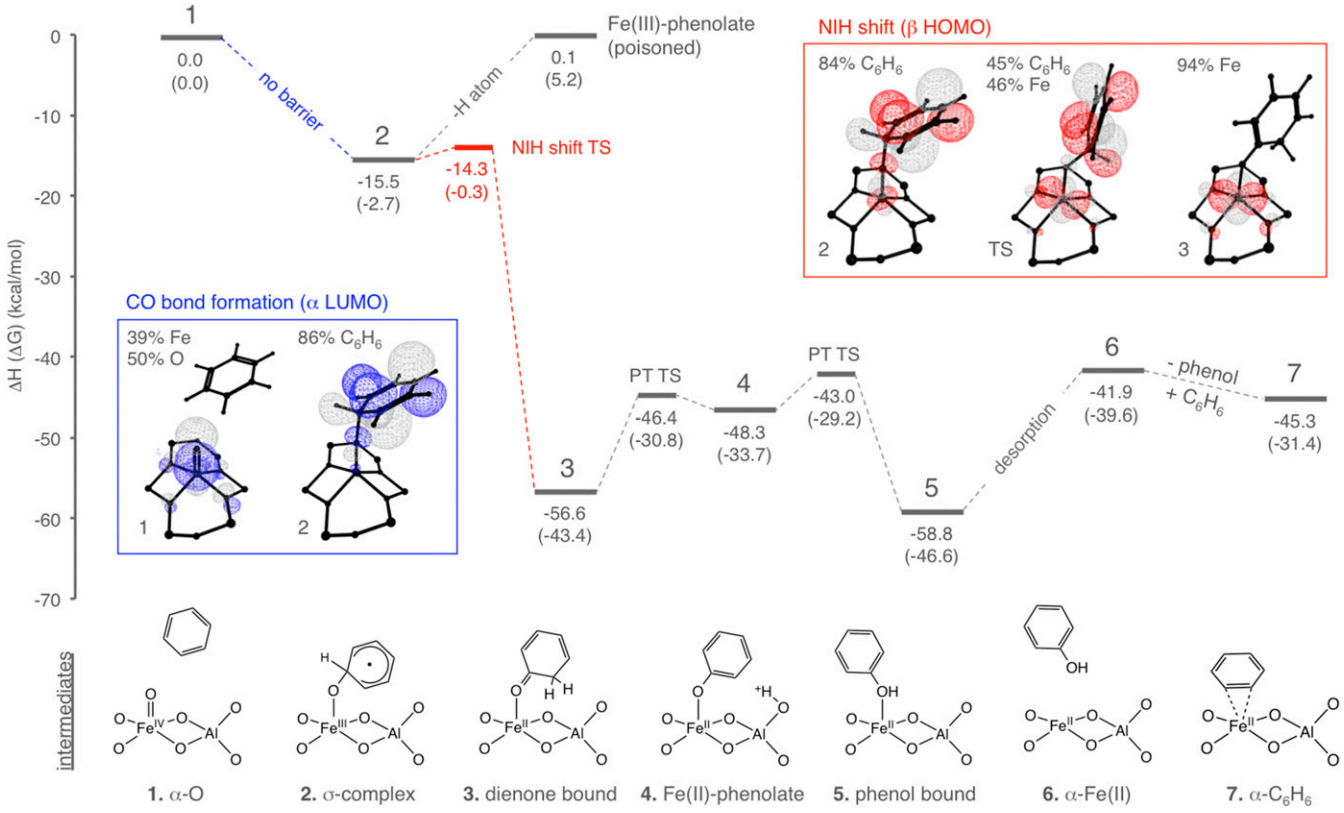

Fig. 4. DFT reaction coordinate for benzene hydroxylation by α-O on the S = 2 surface. Enthalpy changes are given relative to (1) –α-O and gas-phase C_6H_6. The associated free-energy changes (ΔG at 300 K) are reported in parentheses. In the first step of this reaction coordinate, α-O (1) oxidizes C_6H_6 by one electron to form an Fe(III) σ-complex (2). The evolution of the α-LUMO during this electron transfer is shown in the blue inset. The σ-complex undergoes an NIH shift (formal 1,2-hydride shift) to form an Fe(II)-dienone product (3). The evolution of the highest occupied molecular orbital (β-HOMO) during this second electron transfer is shown in the red inset. The dienone rearranges to phenol (4, 5), and then desorbs regenerating α-Fe(II) (6), which binds benzene to form α-C_6H_6 (7).

site, as required by experiment. Reactivity occurs entirely on the S = 2 surface (*SI Appendix*, Fig. S10), and starts with electrophilic attack of α-O (intermediate 1 in Fig. 4) on C_6H_6. As shown in the blue inset, an electron is transferred from C_6H_6 into the Fe $3d_{z^2}$-derived lowest unoccupied molecular orbital (α-LUMO) of α-O in this step, forming a new C–O bond. The resulting σ-complex (intermediate 2) contains an S = 5/2 Fe(III) antiferromagnetically coupled to an S = 1/2 substrate radical. A significant and unique reactivity feature of α-O is the absence of a barrier for CO bond formation. [In contrast, this is the rate-limiting step for electrophilic aromatic hydroxylation in Fe metalloenzymes (29–31) and homogeneous catalysts (32).] From the analysis presented in *SI Appendix*, *SI Methods*, two factors contribute to the elimination of this barrier in the reaction of α-O with C_6H_6. First, the reduction potential of α-O is unusually high (11), contributing an additional ∼20-kcal/mol driving force for C–O bond formation relative to other Fe(IV)=O intermediates. Second, the Fe=O bond of α-O is unusually covalent (10, 11), leading to a frontier molecular orbital that is intrinsically activated for electrophilic chemistry (9–11). Both factors derive from the "entatic state" (33) of α-O defined in previous studies, where rigid constraints from the zeolite lattice enforce an otherwise unstable square pyramidal coordination geometry for this S = 2 Fe(IV)=O site with no axial ligand (9–11).

Proceeding from the σ-complex, an NIH shift (formal 1,2-hydride shift) (34) would occur with a low barrier ($\Delta H^{\ddagger}$ = 1.2 kcal/mol). This is a generally observed mechanism of aromatic hydroxylation by Fe(IV)=O intermediates (16, 29–31). This NIH shift induces transfer of a second electron from the substrate (see Fig. 4, red inset), forming 2,4-cyclohexadienone bound to the reduced Fe(II) active site (intermediate 3). The NIH-shift barrier is the highest on the reaction coordinate, leading to a predicted hydrogen/deuterium kinetic isotope effect (H/D KIE) of α = 1.00–1.16 (see *Materials and Methods* for detail). This is in agreement with the experimental intramolecular α=1.04–1.06 measured by Dubkov et al. (35), but different from the inverse KIEs of α = 0.8–0.9 typically observed with other Fe(IV)=O intermediates (32), where C–O bond formation is rate limiting. Alternative, disfavored mechanisms are evaluated and discussed in *SI Appendix*, *SI Methods*.

While reduction to Fe(II) is facile, our experiments show a small amount of Fe(III) phenolate is also formed during productive turnover. DFT calculations support a strong Fe–O_{C6H5} bond in this poisoned active site ($d_{Fe\text{-}O}$ = 1.79 Å), consistent with rR. This species can be generated by homolyzing the ipso C–H bond of the σ-complex (intermediate 2), which is very weak (bond dissociation enthalpy = 15.6 kcal/mol), suggesting H-atom loss from the bound substrate as a potential poisoning mechanism. We reacted α-O with deuterated substrate to evaluate this mechanism, which predicts an H/D KIE of 1.44–2.89 (see *SI Appendix*, *SI Methods* for detail). As shown in *SI Appendix*, Fig. S9, the reaction of α-O with C_6D_6 results in a 30 ± 5% decrease in the Fe(III)-phenolate DR-UV-vis feature, reflecting an H/D KIE of α = 1.33–1.54 in agreement with the predicted value.

Proceeding from intermediate 3 in Fig. 4, the zeolite lattice can catalyze the tautomerization of the dienone to phenol. A potential mechanism would involve transfer of a proton from the dienone to one of the two adjacent Al T sites (intermediate 4),

and then back to the substrate to yield the phenol-bound Fe(II) active site (intermediate 5). The stabilities of the dienone- and phenol-bound active sites are similar ($\Delta\Delta H$ = 2.2 kcal/mol), despite the 13.9-kcal/mol destabilization of the free dienone relative to phenol. The Fe(II) active site therefore binds the dienone more strongly (ΔH_{des} = 28.6 kcal/mol, versus 16.9 kcal/mol for phenol), potentially disfavoring the premature release of this more reactive species. Phenol then desorbs, regenerating α-Fe(II) (intermediate 6). Alternatively, the dienone may be released from the active site and tautomerize to phenol elsewhere, in a process catalyzed by a remote Brønsted site. Finally, excess benzene present in the reactant stream is calculated to bind weakly to α-Fe(II) ($\Delta H = -3.4$ kcal/mol) to form α-C_6H_6—the species observed experimentally after single turnover.

Conclusion

This study applies advanced spectroscopic techniques to define the mechanism of benzene hydroxylation and Fe(III)-phenolate poisoning in Fe zeolites. A key finding is that the RT reaction of benzene with the Fe(IV)=O intermediate α-O in fact regenerates the reduced α-Fe(II) active site, explaining how catalysis is possible for this Fe-zeolite system. This requires that benzene is hydroxylated through an associative electrophilic mechanism. We find the phenol product desorbs from the active site, but TPD experiments show it remains bound to the catalyst surface. This elucidates the mechanism of productive turnover. At the same time, a small fraction (0.2–5%) of partially oxidized, catalytically inactivated Fe(III)-phenolate sites are formed, further defining a mechanism of active site poisoning.

Experimental data coupled to DFT calculations indicate Fe(III)-phenolate formation occurs through H-atom loss from a bound catalytic intermediate—likely the α-O-C_6H_6 σ-complex (intermediate 2 in Fig. 4), which has a very weak ipso C–H bond. This mechanism, which is entropically favored (over the NIH shift), would be favored at high temperatures. Our data show high temperatures are not required to desorb phenol from the active site, but do aid in desorption of product from the zeolite lattice. Moving from BEA or ZSM-5 to a different zeolite lattice that adsorbs phenol less strongly could enhance catalysis, enabling a lower-temperature process to minimize Fe(III)-phenolate and coke formation. DFT calculations provide further insight into the experimentally defined mechanism for productive turnover. Due to the extreme reactivity of α-O, there is no rate-limiting barrier for aromatic hydroxylation (Fig. 4). Reactivity data from Fe-ZSM-5 show the apparent rate of benzene hydroxylation is in fact 19× greater than that of phenol hydroxylation (2). Combined, these insights suggest benzene is hydroxylated selectively due to its more rapid diffusion through the zeolite lattice—even at high levels of conversion. This model is supported by studies that show the diffusivity of phenol through zeolite lattices is significantly diminished relative to benzene due to its greater polarity (36). Thus, by embedding a highly reactive active site in a matrix that selectively limits the diffusion of the product, it is possible to achieve high conversion and selectivity simultaneously. These mechanistic insights elucidate the remarkable performance of Fe-zeolite catalysts in selective hydrocarbon oxidation. It will be important to explore how these insights can be used to enhance the catalytic hydroxylation of inert hydrocarbons in microporous materials.

Materials and Methods

Zeolite samples were prepared as described in refs. 10 and 11. XAS data were collected at beam lines 7–3 and 9–3 at the Stanford Synchrotron Radiation Lightsource (SSRL) under ring operating conditions of 500 mA over an energy range of 6,785–7,876 eV (k = 14 Å^{-1}). NRVS spectra were collected at the Advanced Photon Source (APS) in Argonne, IL, at beamline 3-ID-D. DFT calculations were performed using the Gaussian 09 software package (see *SI Appendix* for citation). Details on sample preparation and spectroscopic experiments (DR-UV-vis, rR, MCD) are included in *SI Appendix*.

ACKNOWLEDGMENTS. B.E.R.S. acknowledges support from National Science Foundation Graduate Research Fellowship Program Grant DGE-11474 and from the Munger, Pollock, Reynolds, Robinson, Smith & Yoedicke Stanford Graduate Fellowship. M.L.B. acknowledges the Research Foundation – Flanders for funding of his stay at Stanford University (Grant V417018N). R.G.H. acknowledges a Gerhard Casper Stanford Graduate Fellowship. P.V. acknowledges Research Foundation – Flanders (Grant 12L0715N) and Katholieke Universiteit Leuven for his postdoctoral fellowships and travel grants during his stay at Stanford University. Funding for this work was provided by National Science Foundation Grant CHE-1660611 (to E.I.S.) and Research Foundation – Flanders Grant G0A2216N (to B.F.S.). Use of the Stanford Synchrotron Radiation Lightsource, SLAC National Accelerator Laboratory, is supported by the US Department of Energy (DOE), Office of Science, Office of Basic Energy Sciences under Contract DE-AC02-76SF00515. The SSRL Structural Molecular Biology Program is supported by the DOE Office of Biological and Environmental Research and by National Institutes of Health, National Institute of General Medical Sciences Grant P41GM103393 (to K.O.H.). This research used resources of the APS, a US DOE Office of Science User Facility operated for the DOE Office of Science by Argonne National Laboratory under Contract DE-AC02-06CH11357.

1. Manfred W, Markus W, Michael K (2004) *Ullmann's Encyclopedia of Industrial Chemistry* (Wiley-VCH GmbH & Co., Weinheim, Germany).
2. Ivanov AA, et al. (2003) Kinetics of benzene to phenol oxidation over Fe-ZSM-5 catalyst. *Appl Catal A Gen* 249:327–343.
3. Notté PP (2000) The AlphOx^{TM} process or the one-step hydroxylation of benzene into phenol by nitrous oxide. Understanding and tuning the ZSM-5 catalyst activities. *Top Catal* 13:387–394.
4. Parmon VN, Panov GI, Uriarte A, Noskov AS (2005) Nitrous oxide in oxidation chemistry and catalysis: Application and production. *Catal Today* 100:115–131.
5. Mizuno N (2009) *Modern Heterogeneous Oxidation Catalysis: Design, Reactions and Characterization* (John Wiley & Sons, Weinheim, Germany).
6. Xin H, et al. (2009) A hierarchical Fe/ZSM-5 zeolite with superior catalytic performance for benzene hydroxylation to phenol. *Chem Commun (Camb)* 2009:7590–7592.
7. Elias K, Andreas R, Bernd V (2008) *Direct Ring Oxidation of Aromatics to Phenols. Handbook of Heterogeneous Catalysis* (American Cancer Society), pp 3433–3448.
8. Guisnet M, Ribeiro FR (2011) *Deactivation and Regeneration of Zeolite Catalysts* (Imperial College Press, London).
9. Snyder BER, Bols ML, Schoonheydt RA, Sels BF, Solomon EI (2018) Iron and copper active sites in zeolites and their correlation to metalloenzymes. *Chem Rev* 118:2718–2768.
10. Snyder BER, et al. (2016) The active site of low-temperature methane hydroxylation in iron-containing zeolites. *Nature* 536:317–321.
11. Snyder BER, et al. (2018) Structural characterization of a non-heme iron active site in zeolites that hydroxylates methane. *Proc Natl Acad Sci USA* 115:4565–4570.
12. Scheidt WR, Durbin SM, Sage JT (2005) Nuclear resonance vibrational spectroscopy–NRVS. *J Inorg Biochem* 99:60–71.
13. Yoshizawa K, Shiota Y, Yumura T, Yamabe T (2000) Direct methane-methanol and benzene-phenol conversions on Fe–ZSM-5 zeolite: Theoretical predictions on the reaction pathways and energetics. *J Phys Chem B* 104:734–740.
14. Kachurovskaya NA, Zhidomirov GM, Hensen EJM, van Santen RA (2003) Cluster model DFT study of the intermediates of benzene to phenol oxidation by N2O on FeZSM-5 zeolites. *Catal Lett* 86:25–31.
15. Ivanov DP, Pirutko LV, Panov GI (2014) Effect of steaming on the catalytic performance of ZSM-5 zeolite in the selective oxidation of phenol by nitrous oxide. *J Catal* 311:424–432.
16. Lindhorst AC, et al. (2017) Mechanistic insights into the biomimetic catalytic hydroxylation of arenes by a molecular Fe(NHC) complex. *J Catal* 352:599–605.
17. de Visser SP, Oh K, Han A-R, Nam W (2007) Combined experimental and theoretical study on aromatic hydroxylation by mononuclear nonheme iron(IV)-oxo complexes. *Inorg Chem* 46:4632–4641.
18. Kang M-J, et al. (2007) Mechanistic insight into the aromatic hydroxylation by high-valent iron(IV)-oxo porphyrin π-cation radical complexes. *J Org Chem* 72: 6301–6304.
19. Fellah MF, Onal I, van Santen RA (2010) A density functional theory study of direct oxidation of benzene to phenol by N_2O on a $[FeO]^{1+}$-ZSM-5 cluster. *J Phys Chem C* 114:12580–12589.
20. Xia H, et al. (2008) Direct spectroscopic observation of Fe(III)–Phenolate complex formed from the reaction of benzene with peroxide species on Fe/ZSM-5 at room temperature. *J Phys Chem C* 112:9001–9005.
21. Li G, et al. (2011) Stability and reactivity of active sites for direct benzene oxidation to phenol in Fe/ZSM-5: A comprehensive periodic DFT study. *J Catal* 284:194–206.
22. Koekkoek AJJ, et al. (2013) Catalytic performance of sheet-like Fe/ZSM-5 zeolites for the selective oxidation of benzene with nitrous oxide. *J Catal* 299:81–89.
23. Meng L, Zhu X, Hensen EJM (2017) Stable Fe/ZSM-5 nanosheet zeolite catalysts for the oxidation of benzene to phenol. *ACS Catal* 7:2709–2719.
24. Panov GI, et al. (1990) The role of iron in N_2O decomposition on ZSM-5 zeolite and reactivity of the surface oxygen formed. *J Mol Catal* 61:85–97.

25. Solomon EI, Pavel EG, Loeb KE, Campochiaro C (1995) Magnetic circular dichroism spectroscopy as a probe of the geometric and electronic structure of non-heme ferrous enzymes. *Coord Chem Rev* 144:369–460.
26. Solomon EI, et al. (2000) Geometric and electronic structure/function correlations in non-heme iron enzymes. *Chem Rev* 100:235–350.
27. Pyrz JW, Roe AL, Stern LJ, Que L, Jr (1985) Model studies of iron-tyrosinate proteins. *J Am Chem Soc* 107:614–620.
28. Carrano CJ, Carrano MW, Sharma K, Backes G, Sanders-Loehr J (1990) Resonance Raman spectra of high- and low-spin ferric phenolates. Models for dioxygenases and nitrile hydratase. *Inorg Chem* 29:1865–1870.
29. Fitzpatrick PF (2003) Mechanism of aromatic amino acid hydroxylation. *Biochemistry* 42:14083–14091.
30. Neidig ML, et al. (2006) Spectroscopic and electronic structure studies of aromatic electrophilic attack and hydrogen-atom abstraction by non-heme iron enzymes. *Proc Natl Acad Sci USA* 103:12966–12973.
31. Bassan A, Blomberg MR, Siegbahn PE (2003) Mechanism of aromatic hydroxylation by an activated FeIV=O core in tetrahydrobiopterin-dependent hydroxylases. *Chemistry* 9:4055–4067.
32. Nam W (2007) High-valent iron(IV)-oxo complexes of heme and non-heme ligands in oxygenation reactions. *Acc Chem Res* 40:522–531.
33. Vallee BL, Williams RJ (1968) Metalloenzymes: The entatic nature of their active sites. *Proc Natl Acad Sci USA* 59:498–505.
34. Guroff G, et al. (1967) Hydroxylation-induced migration: The NIH shift. Recent experiments reveal an unexpected and general result of enzymatic hydroxylation of aromatic compounds. *Science* 157:1524–1530.
35. Dubkov KA, et al. (1997) Kinetic isotope effects and mechanism of biomimetic oxidation of methane and benzene on FeZSM-5 zeolite. *J Mol Catal Chem* 123:155–161.
36. Moore RM, Katzer JR (1972) Counterdiffusion of liquid hydrocarbons in type Y zeolite: Effect of molecular size, molecular type, and direction of diffusion. *AIChE J* 18:816–824.